

Generative Adversarial Networks for Robust Cryo-EM Image Denoising

Hanlin Gu · Yin Xian · Ilona Christy Unarta · Yuan Yao

Received: date / Accepted: date

Contents

Introduction	2
Robust Denoising in Deep Learning	2
Challenges of Cryo-EM Image Denoising	3
Outline	4
Background: Data Representation and Mapping	5
Autoencoder	5
GAN	5
JS-GAN	6
WGAN and WGANgp	6
Robust Denoising Method	6
Huber Contamination Noise Model	6
Robust Denoising method	7
Robust Recovery via β -GAN	8
Robust Recovery Theory	8
Stablized Robust Denoising by Joint Autoencoder and β -GAN	9
Stability of combining Autoencoder into GAN	10
Application: Robust Denoising of Cryo-EM Images	11
Datasets	11
RNAP: Simulation Dataset	11
EMPIAR-10028: Real Dataset	12
Evaluation Method	12
Network Architecture and Hyperparameter	14
Results for RNAP	14

This research made use of the computing resources of the X-GPU cluster supported by the Hong Kong Research Grant Council Collaborative Research Fund: C6021-19EF. The research of Hanlin Gu and Yuan Yao is supported in part by HKRGC 16308321, ITF UIM/390, as well as awards from Tencent AI Lab and Si Family Foundation. We would like to thank Dr. Xuhui Huang for helpful discussions.

Hanlin Gu
 Hong Kong University of Science and Technology, Hong Kong SAR China.
 E-mail: hguaf@connect.ust.hk

Yin Xian
 Hong Kong Applied Science and Technology Research Institute (ASTRI), Hong Kong SAR China.
 E-mail: poline3939@gmail.com

Ilona Christy Unarta
 Hong Kong University of Science and Technology, Hong Kong SAR China.
 E-mail: icunarta@connect.ust.hk

Yuan Yao
 Hong Kong University of Science and Technology, Hong Kong SAR China.
 E-mail: yuany@ust.hk

Denoising without contamination	14
Robustness under contamination	15
Results for EMPIAR-10028	17
Conclusion and Discussion	17
Appendix	18
Reference	23

Abstract The Cryo-Electron Microscopy (Cryo-EM) becomes popular for macromolecular structure determination. However, the 2D images captured by Cryo-EM are of high noise and often mixed with multiple heterogeneous conformations and contamination, imposing a challenge for denoising. Traditional image denoising methods and simple Denoising Autoencoder cannot work well when the Signal-to-Noise Ratio (SNR) of images is meager and contamination distribution is complex. Thus it is desired to develop new effective denoising techniques to facilitate further research such as 3D reconstruction, 2D conformation classification, and so on. In this chapter, we approach the robust denoising problem for Cryo-EM images by introducing a family of Generative Adversarial Networks (GAN), called β -GAN, which is able to achieve robust estimation of certain distributional parameters under Huber contamination model with statistical optimality. To address the denoising challenges, for example, the traditional image generative model might be contaminated by a small portion of unknown outliers, β -GANs are exploited to enhance the robustness of Denoising Autoencoder. Our proposed method is evaluated by both a simulated dataset on the Thermus aquaticus RNA Polymerase (RNAP) and a real world dataset on the Plasmodium falciparum 80S ribosome dataset (EMPIAR-10028), in terms of Mean Square Error (MSE), Peak Signal-to-Noise Ratio (PSNR), Structural Similarity Index Measure (SSIM) and 3D Reconstruction as well. Quantitative comparisons show that equipped with some designs of β -GANs and the robust ℓ_1 -Autoencoder, one can stabilize the training of GANs and achieve the state-of-the-art performance of robust denoising with low SNR data and against possible information contamination. Our proposed methodology thus provides an effective tool for robust denoising of Cryo-EM 2D images, and helpful for 3D structure reconstruction.

Keywords Generative adversarial networks · Autoencoder · Robust statistics · Denoising · Cryo-EM

Introduction

Robust Denoising in Deep Learning

Deep learning technique has rapidly entered into the field of image processing. One of the most popular methods was the Denoising Autoencoder (DA) motivated by [Vincent et al. \(2008\)](#). It used the reference data to learn a compressed representation (encoder) for the dataset. One extension of DA was presented in [Xie et al. \(2012\)](#), which exploited the sparsity regularization and the reconstruction loss to avoid over-fitting. Other developments, such as [Zhang et al. \(2017\)](#), made use of the residual network architecture to improve the quality of denoised images. In addition, [Agostinelli et al. \(2013\)](#) combined several sparse Denoising Autoencoder to enhance the robustness under different noise.

The Generative Adversarial Networks (GAN) recently gained its popularity and provides a promising new approach for image denoising. GAN was proposed by [Goodfellow et al. \(2014\)](#), and was mainly composed of two parts: the generator (G : generate the new samples) and the discriminator (D : determine whether the samples are real or generated (fake)). Original GAN ([Goodfellow et al. \(2014\)](#)) aimed to minimize the Jensen-Shannon (JS) divergence between distributions of the generated samples and the true samples, hence called JS-GAN. Various GANs were then studied, and in particular, [Arjovsky et al. \(2017\)](#) proposed the Wasserstein GAN (WGAN), which replaced the JS divergence with Wasserstein distance. [Gulrajani et al. \(2017\)](#) further improved the WGAN with the gradient penalty that stabilized the model training. For image denoising problem, GAN could better describe the distribution of original data by exploiting the common information of samples. Consequently, GANs were

widely applied in the image denoising problem (Tran et al. (2020); Tripathi et al. (2018); Yang et al. (2018); Chen et al. (2018); Dong et al. (2020)).

Recently, Gao et al. (2019, 2020) showed that a general family of GANs (β -GANs, including JS-GAN and TV-GAN) enjoyed robust reconstruction when the data sets contain outliers under Huber contamination models (Huber (1992)). In this case, observed samples are drawn from a complex distribution, which is a mixture of contamination distribution and real data distribution. A particular example is provided by Cryo-Electron Microscopy (Cryo-EM) imaging, where the original noisy images are likely contaminated with outliers as broken or non-particles. The main challenges of Cryo-EM image denoising are summarized in the subsequent section.

Challenges of Cryo-EM Image Denoising

The Cryo-Electron Microscopy (Cryo-EM) has become one of the most popular techniques to resolve the atomic structure. In the past, Cryo-EM was limited to large complexes or low-resolution models. Recently the development of new detector hardware has dramatically improved the resolution in Cryo-EM (Kühlbrandt (2014)), which made Cryo-EM widely used in a variety of research fields. Different from X-ray crystallography (Warren (1990)), Cryo-EM had the advantage of preventing the recrystallization of inherent water and re-contamination. Also, Cryo-EM was superior to Nuclear Magnetic Resonance spectroscopy (Wüthrich (1986)) in solving macromolecules in the native state. In addition, both X-ray crystallography and Nuclear Magnetic Resonance spectroscopy required large amounts of relatively pure samples, whereas Cryo-EM required much fewer samples (Bai et al. (2015)). For this celebrated development of Cryo-EM for the high-resolution structure determination of biomolecules in solution, the Nobel Prize in Chemistry in 2017 was awarded to three pioneers in this field (Shen (2018)).

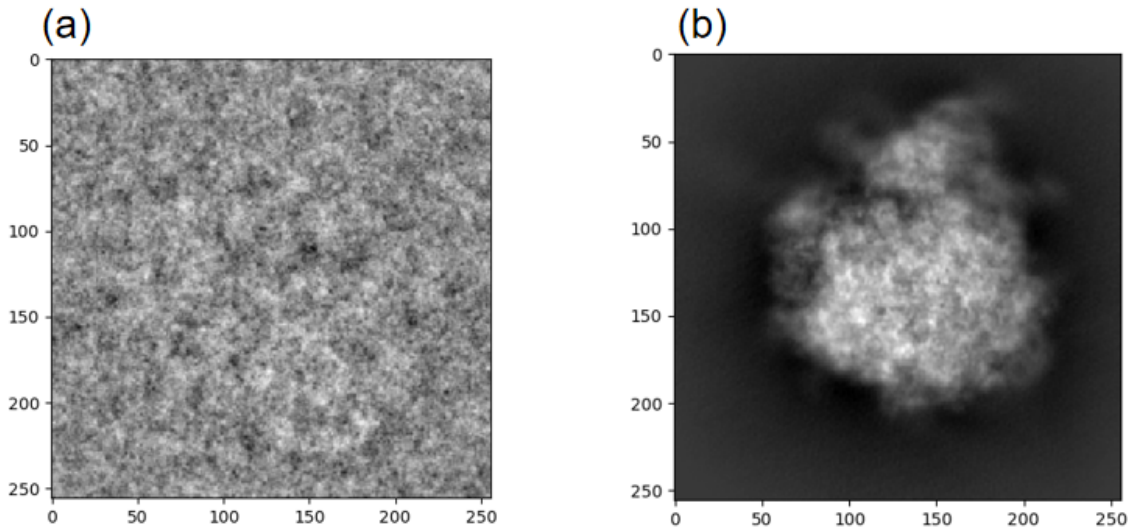


Fig. 1: (a) a noisy Cryo-EM image (b) a reference image

However, it is a computational challenge in processing raw Cryo-EM images, due to heterogeneity in molecular conformations and high noise. Macromolecules in natural conditions are usually heterogeneous, i.e., multiple metastable structures might coexist in the experimental samples (Frank

(2006); Scheres (2016)). Such conformational heterogeneity adds extra difficulty to the structural reconstruction as we need to assign each 2D image to not only the correct projection angle but also its corresponding conformation. This imposes a computational challenge that one needs to denoise the Cryo-EM images without losing the key features of their corresponding conformations. Moreover, in the process of generating Cryo-EM images, one needs to provide a view using the electron microscope for samples that are in frozen condition. Thus there are two types of noise: one is from ice, and the other is from the electron microscope. Both of them are significant in contributing high noise in Cryo-EM images and leave a difficulty to the detection of particle structures (Fig. 1 shows a typical noisy Cryo-EM image with its reference image, which is totally non-identifiable to human eyes). In extreme cases, some experimental images even do not contain any particles, rendering it difficult for particle picking either manually or automatically (Wang et al. (2016)). How to achieve robust denoising against such kind of contamination thus becomes a critical problem. Therefore, it is a great challenge to develop robust denoising methods for Cryo-EM images to reconstruct heterogeneous biomolecular structures.

There are a plethora of denoising methods developed in applied mathematics and machine learning that could be applied to Cryo-EM image denoising. Most of them in Cryo-EM are based on unsupervised learning, which don't need any reference image data to learn. Wang and Yin (2013) proposed a filtering method based on non-local means, which made use of the rotational symmetry of some biological molecules. Also, Wei and Yin (2010) designed the adaptive non-local filter, which made use of a wide range of pixels to estimate the denoised pixel values. Besides, Xian et al. (2018) compared transform domain filtering method: BM3D (Dabov et al. (2007)) and dictionary learning method: KSVD (Aharon et al. (2006)) in denoising problem in Cryo-EM. However, all of these didn't work well in low Signal-to-Noise Ratio (SNR) situations. In addition, Covariance Wiener Filtering (CWF) (Bhamre et al. (2016)) was proposed for image denoising. However, CWF needed large sample size of data in order to estimate the covariance matrix correctly, although it had an attractive denoising effect. Therefore, a robust denoising method in Cryo-EM images was needed.

Outline

In this chapter, we propose a robust denoising scheme of Cryo-EM images by exploiting joint training of both Autoencoders and a new type of GANs β -GANs. Our main results are summarized as follows.

- Both Autoencoder and GANs help each other for Cryo-EM denoising in low Signal-to-Noise Ratio scenarios. On the one hand, Autoencoder helps stabilize GANs during training, without which the training processes of GANs are often collapsed due to high noise; on the other hand, GANs help Autoencoder in denoising by sharing information in similar samples via distribution learning. For example, WGAN combined with autoencoder often achieve state-of-the-art performance due to its ability of exploiting information in similar samples for denoising.
- To achieve robustness against partial contamination of samples, one needs to choose both robust reconstruction loss for Autoencoder (e.g., ℓ_1 loss) and robust β -GANs (e.g., (.5, .5)-GAN or (1, 1)-GAN¹, which is proved to be robust against Huber contamination), that achieve competitive performance with WGANs in contamination-free scenarios, but do not deteriorate that much with data contamination.
- Numerical experiments are conducted with both a heterogeneous conformational dataset on the *Thermus aquaticus* RNA Polymerase (RNAP) and a homogenous dataset on the *Plasmodium falciparum* 80S ribosome dataset (EMPIAR-10028). The experiments on those datasets show the validity of the proposed methodology and suggest that: while WGAN, (.5, .5)-GAN, and (1, 1)-GAN combined with ℓ_1 -Autoencoder are among the best choices in contamination-free cases, the latter two are overall the most recommended for robust denoising.

¹ β -GAN has two parameters: α and β , written as (α, β) -GAN in this chapter.

To achieve the goals above, this chapter is to provide an overview on various developments of GANs with their robustness properties. After that we focus on the application to the challenge of Cryo-EM image robust denoising problem.

The chapter is structured as follows. In section “**Background: Data Representation and Mapping**”, we provide a general overview of Autoencoder and GAN. In section “**Robust Denoising Method**”, we model the tradition denoising problem based on Huber contamination firstly and discuss β -GAN and its statistics. Finally, we give our algorithm based on combination of β -GAN and Autoencoder, which is training stable. The evaluation of the algorithm in Cryo-EM data is shown in the section “**Application: Robust Denoising of Cryo-EM Images**”. The section “**Conclusion and Discussion**” concludes the chapter. In addition, we implement the supplementary experiment in the section “**Appendix**”.

Background: Data Representation and Mapping

Efficient representation learning of data distribution is crucial for many machine learning based model. For a set of the real data samples X , the classical way to learn the probability distribution of this data (P_r) is to find P_θ by minimizing the distance between P_r and P_θ , such as Kullback-Leibler divergence $D_{KL}(P_r||P_\theta)$. This means we can pass a random variable through a parametric function to generate samples following a certain distribution P_θ instead of directly estimating the unknown distribution P_r . By varying θ , we can change this distribution and make it close to the real data distribution P_r . Autoencoder and GANs are two well known methods in data representation. Autoencoder is good at learning the representation of data with low dimensions with an explicit characterization of P_θ , while GAN offers flexibility in defining the objective function (such as the Jensen-Shannon divergence) by directly generating samples without explicitly formulating P_θ .

Autoencoder

Autoencoder (Baldi (2012)) is a type of neural network used to learn efficient codings of unlabeled data. It learns a representation (encoding) for a set of data, typically for dimensional reduction by training the network. An Autoencoder has two main parts: encoder and decoder. The encoder maps the input data $x (\in X)$ into a latent representation z , while the decoder map the latent representation back to the data space:

$$z \sim \text{Enc}(x) \quad (1)$$

$$\hat{x} \sim \text{Dec}(z). \quad (2)$$

Autoencoders are trained to minimized reconstruction errors, such as: $\mathcal{L}(x, \hat{x}) = ||x - \hat{x}||^2$.

Various techniques have been developed to improve data representation ability for Autoencoder, such as imposing regularization on the encoding layer:

$$\mathcal{L}(x, \hat{x}) + \Omega(h), \quad (3)$$

where h is the mapping function of the encoding layer, and $\Omega(h)$ is the regularization term. The Autoencoder is good at data denoising and dimension reduction.

GAN

The Generative Adversarial Network (GAN), firstly proposed by Goodfellow (Goodfellow et al. (2014), called JS-GAN), is a class of machine learning framework. The goal of GAN is to learn to generate new data with the same statistics as the training set. Though original GAN is proposed as a form of

generative model for unsupervised learning, GAN has proven useful for semi-supervised learning, fully supervised learning and reinforcement learning (Hua et al. (2019); Sarmad et al. (2019); Dai et al. (2017)).

Although GAN has shown great success in machine learning, the training of GAN is not easy, and is known to be slow and unstable. The problems of GAN (Bau et al. (2019); Arjovsky et al. (2017)) include:

- *Hard to achieve Nash equilibrium.* The updating process of the generator and the discriminator models are hard to guarantee a convergence.
- *Vanishing gradient.* The gradient update is slow when the discriminator is well trained.
- *Mode collapse.* The generator fails to generate samples with enough representative.

JS-GAN

JS-GAN proposed in Goodfellow et al. (2014) took Jensen-Shannon (JS) distance to measure the difference between different data distribution. The mathematics expression is follows:

$$\min_G \max_D \mathbb{E}_{x \sim P(X), z \sim P(Z)} [\log D(x) + \log(1 - D(G(z)))], \quad (4)$$

where G is a generator which maps disentangled noise $z \sim P(Z)$ (usually Gaussian $N(0, I)$) to fake image data in an purpose to confuse the discriminator D from real data. The discriminator D is simply a classifier, which makes an effort to distinguish real data from the fake data generated by G . $P(X)$ is the input data distribution. z is noise. $P(Z)$ is the noise distribution, and it is used for data generation. GAN trains the adversarial process by updating generator and the discriminator, where training the generator in succeeding in fooling the discriminator.

WGAN and WGANgp

Wasserstein GAN (Arjovsky et al. (2017)) replaced the JS distance with the Wasserstein distance:

$$\min_G \max_D \mathbb{E}_{x \sim P(X), z \sim P(Z)} \{D(x) - D(G(z))\}. \quad (5)$$

In reality, WGAN applied weight clipping of neural network to satisfies Lipschitz condition for discriminator. Moreover, Gulrajani et al. (2017) proposed WGANgp based on WGAN, which introduced a penalty in gradient to stabilize the training.

$$\min_G \max_D \mathbb{E}_{(x,z) \sim P(X,z)} \{D(x) - D(G(z)) + \mu \mathbb{E}_{\tilde{x}} (\|\nabla_{\tilde{x}} D(\tilde{x})\|_2 - 1)^2\}, \quad (6)$$

where \tilde{x} is uniformly sampled along straight lines connecting pairs of the generated and real samples; and μ is a weighting parameter. In WGANgp, the last layer of the sigmoid function in the discriminator network is removed. Thus D 's output range is the whole real \mathbb{R} , but its gradient is close to 1 to achieve Lipschitz-1 condition.

Robust Denoising Method

Huber Contamination Noise Model

Let $x \in \mathbb{R}^{d_1 \times d_2}$ be a clean image, often called reference image in the sequel. The generative model of noisy image $y \in \mathbb{R}^{d_1 \times d_2}$ under the linear, weak phase approximation (Bhamre et al. (2016)) could be described by

$$y = a * x + \zeta, \quad (7)$$

where $*$ denotes the convolution operation, a is the point spread function of the microscope convolving with the clean image and ζ is an additive noise, usually assumed to be Gaussian noise that corrupts the image. In order to remove the noise the microscope brings, traditional Denoising Autoencoder could be exploited to learn from examples $(y_i, x_i)_{i=1, \dots, n}$ the inverse mapping a^{-1} from the noisy image y to the clean image x .

However, this model is not sufficient in the real case. In the experimental data, the contamination will significantly affect the denoising efficiency if the denoising methods continuously depend on the sample outliers. Therefore we introduce the following Huber contamination model to extend the image formation model (see Eq. (7)).

Consider that the pair of reference image and experimental image (x, y) is subject to the following mixture distribution P_ϵ :

$$P_\epsilon = (1 - \epsilon)P_0 + \epsilon Q, \quad \epsilon \in [0, 1], \quad (8)$$

a mixture of true distribution P_0 of probability $(1 - \epsilon)$ and arbitrary contamination distribution Q of probability ϵ . P_0 is characterized by Eq. (7) and Q accounts for the unknown contamination distribution possibly due to ice, broken of data, and so on such that the image sample does not contain any particle information. This is called the Huber contamination model in statistics [Huber \(1992\)](#). Our purpose is that given n samples $(x_i, y_i) \sim P_\epsilon$ ($i = 1, \dots, n$), possibly contaminated with unknown Q , learn a robust inverse map $a^{-1}(y)$.

Robust Denoising method

Exploiting a neural network to approximate the robust inverse mapping $G_\theta : \mathbb{R}^{d_1 \times d_2} \rightarrow \mathbb{R}^{d_1 \times d_2}$. The neural network is parameterized by $\theta \in \Theta$. The goal is to ensure that discrepancy between reference image x and reconstructed image $\hat{x} = G_\theta(y)$ is small. Such a discrepancy is usually measured by some non-negative loss function: $\ell(x, \hat{x})$. Therefore, the denoising problem minimizes the following expected loss,

$$\arg \min_{\theta \in \Theta} \mathcal{L}(\theta) := \mathbb{E}_{x, y}[\ell(x, G_\theta(y))]. \quad (9)$$

In practice, given a set of training samples $S = \{(x_i, y_i) : i = 1, \dots, n\}$, we aim to solve the following empirical loss minimization problem,

$$\arg \min_{\theta \in \Theta} \hat{\mathcal{L}}_S(\theta) := \frac{1}{n} \sum_{i=1}^n \ell(x_i, G_\theta(y_i)). \quad (10)$$

the following choices of loss functions are considered:

- (**ℓ_2 -Autoencoder**) $\ell(x, \hat{x}) = \frac{1}{2} \|x - \hat{x}\|_2^2 := \frac{1}{2} \sum_{i,j} (x_{ij} - \hat{x}_{ij})^2$, or $\mathbb{E}\ell(x, \hat{x}) = D_{KL}(p(x) \| q(\hat{x}_\theta))$ equivalently, where $\hat{x}_\theta \sim \mathcal{N}(x, \sigma^2 I_D)$;
- (**ℓ_1 -Autoencoder**) $\ell(x, \hat{x}) = \|x - \hat{x}\|_1 := \sum_{i,j} |x_{ij} - \hat{x}_{ij}|$, or $\mathbb{E}\ell(x, \hat{x}) = D_{KL}(p(x) \| q(\hat{x}_\theta))$ equivalently, where $\hat{x}_\theta \sim \text{Laplace}(x, b)$;
- (**Wasserstein-GAN**) $\ell(x, \hat{x}) = W_1(p(x), q_\theta(\hat{x}))$, where W_1 is the 1-Wasserstein distance between distributions of x and \hat{x} ;
- (**β -GAN**) $\ell(x, \hat{x}) = D(p(x) \| q_\theta(\hat{x}))$, where D is some divergence function to be discussed below between distributions of x and \hat{x} .

Both the ℓ_2 and ℓ_1 losses consider the reconstruction error of G_θ . The ℓ_2 -loss above is equivalent to assume that $G_\theta(y|x)$ follows a Gaussian distribution $\mathcal{N}(x, \sigma^2 I_D)$, and the ℓ_1 -loss instead assumes a Laplacian distribution centered at x . As a result, the ℓ_2 -loss pushes the reconstructed image \hat{x} toward mean by averaging out the details and thus blurs the image. On the other hand, the ℓ_1 -loss pushes \hat{x} toward the coordinate-wise median, keeping the majority of details while ignoring some large deviations. It improves the reconstructed image, and more robust than the ℓ_2 loss against large outliers. Although ℓ_1 -Autoencoder has a more robust loss than ℓ_2 , both of them are not sufficient to handle the contamination. In the framework of the Huber contamination model (Eq. (8)), β -GAN is introduced below.

Robust Recovery via β -GAN

Recently Gao et al. (2019, 2020) came up with a more general form of β -GAN. It aims to solve the following minimax optimization problem to find the G_θ ,

$$\min_{G_\theta} \max_D \mathbb{E}[S(D(x), 1) + S(D(G_\theta(y)), 0)], \quad (11)$$

where $S(t, 1) = -\int_t^1 c^{\alpha-1}(1-c)^\beta dc$, $S(t, 0) = -\int_0^t c^\alpha(1-c)^{\beta-1} dc$, $\alpha, \beta \in [-1, 1]$. For simplicity, we denote this family with parameters α, β by (α, β) -GAN in this chapter.

The family of (α, β) -GAN includes many popular members. For example, when $\alpha = 0, \beta = 0$, it becomes the JS-GAN (Goodfellow et al. (2014)), which aims to solve the minimax problem (Eq. (4)) whose loss is the Jensen-Shannon divergence. When $\alpha = 1, \beta = 1$ the loss is a simple mean square loss; when $\alpha = -0.5, \beta = -0.5$, the loss is boost score.

However, the Wasserstein GAN (WGAN) is not a member of this family. By formally taking $S(t, 1) = t$ and $S(t, 0) = -t$, we could derive the type of WGAN as Eq. (5).

Robust Recovery Theory

Extending the traditional image generative model to a Huber contamination model and exploit the β -GAN toward robust denoising under unknown contamination. Below includes a brief introduction to robust β -GAN, which achieves provable robust estimate or recovery under Huber contamination model. Recently, Gao establishes the statistical optimality of β -GANs for robust estimate of mean (location) and covariance (scatter) of the general elliptical distributions (Gao et al. (2019), Gao et al. (2020)). Here we introduce the main results.

Definition 1 (Elliptical Distribution) A random vector $X \in \mathbb{R}^p$ follows an elliptical distribution if and only if it has the representation $X = \theta + \xi AU$, where $\theta \in \mathbb{R}^p$ and $A \in \mathbb{R}^{p \times r}$ are model parameters. The random variable U is distributed uniformly on the unit sphere $\{u \in \mathbb{R}^r : \|u\| = 1\}$ and $\xi \geq 0$ is a random variable in \mathbb{R} independent of U . The vector θ and the matrix $\Sigma = AA^T$ are called the location and the scatter of the elliptical distribution.

Normal distribution is just a member in this family characterized by mean θ and covariance matrix Σ . Cauchy distribution is another member in this family whose moments do not exist.

Definition 2 (Huber contamination model) $X_1, \dots, X_n \stackrel{\text{iid}}{\sim} (1 - \epsilon)P_{ell} + \epsilon Q$, where we consider the P_{ell} an elliptical distribution in its canonical form.

A more general data generating process than Huber contamination model is called the strong contamination model below, as the TV -neighborhood of a given elliptical distribution P_{ell} :

Definition 3 (Strong contamination model) $X_1, \dots, X_n \stackrel{\text{iid}}{\sim} P$, for some P satisfying

$$TV(P, P_{ell}) < \epsilon.$$

Definition 4 (Discriminator Class) Let $\text{sigmoid}(x) = \frac{1}{1+e^{-x}}$, $\text{ramp}(x) = \max(\min(x + 1/2, 1), 0)$, and $\text{ReLU}(x) = \max(x, 0)$. Define a general discriminator class of deep neural nets: firstly define the a ramp bottom layer

$$\mathcal{G}_{\text{ramp}} = g(x) = \text{ramp}(u^t x + b), u \in \mathbb{R}^p, b \in \mathbb{R}. \quad (12)$$

Then, with $\mathcal{G}_1(B) = \mathcal{G}_{\text{ramp}}$, inductively define

$$\mathcal{G}_{l+1}(B) = \left\{ g(x) = \text{ReLU}\left(\sum_{h \geq 1} v_h g_h(x)\right) : \sum_{h \geq 1} |v_h| \leq B, g_h \in \mathcal{G}_l(B) \right\}. \quad (13)$$

Noted that the neighboring two layers are connected via ReLU activation functions. Finally, the network structure is defined by:

$$\mathcal{D}^L(\kappa, B) = \left\{ D(x) = \text{sigmoid} \left(\sum_{j \geq 1} w_j g_j(x) \right) : \sum_{j \geq 1} |w_j| \leq \kappa, g_j \in \mathcal{G}_L(B) \right\}. \quad (14)$$

This is a network architecture consisting of L hidden layers.

Now consider the following β -GAN induced by a proper scoring rule $S : [0, 1] \times \{0, 1\} \rightarrow \mathbb{R}$ with the discriminator class above:

$$(\hat{\theta}, \hat{\Sigma}) = \arg \min_{(\theta, \Sigma)} \max_{D \in \mathcal{D}^L(\kappa, B)} \frac{1}{n} \sum_{i=1}^n S(D(x_i), 1) + \mathbb{E}_{x \sim P_{ell}(\theta, \Sigma)} S(D(x), 0). \quad (15)$$

The following theorem shows that such a β -GAN may give a statistically optimal estimate of location and scatter of the general family of Elliptical distributions under strong contamination models.

Theorem 1 (Gao-Yao-Zhu (Gao et al. (2020))) *Consider the (α, β) -GANs with $|\alpha - \beta| < 1$. The discriminator class $D = \mathcal{D}^L(k, B)$ is specified by Eq. (14). Assume $\frac{p}{n} + \epsilon^2 \leq c$ for some sufficiently small constant $c > 0$. Set $1 \leq L = O(1)$, $1 \leq B = O(1)$, and $\kappa = O(\sqrt{\frac{p}{n}} + \epsilon)$. Then for any $X_1, \dots, X_n \stackrel{iid}{\sim} P$, for some P satisfying $TV(P, P_{ell}) < \epsilon$ with small enough ϵ , we have:*

$$\begin{aligned} \|\hat{\theta} - \theta\|^2 &< C \left(\frac{p}{n} \vee \epsilon^2 \right), \\ \|\hat{\Sigma} - \Sigma\|_{op}^2 &< C \left(\frac{p}{n} \vee \epsilon^2 \right), \end{aligned} \quad (16)$$

with probability at least $1 - e^{-C'(p+n\epsilon^2)}$ (universal constants C and C') uniformly over all $\theta \in R^p$ and all $\|\Sigma\|_{op} \leq M$.

The theorem established that for all $|\alpha - \beta| < 1$, (α, β) -GAN family is robust in the sense that one can learn a distribution P_{ell} from contaminated distributions P_ϵ such that $TV(P_\epsilon, P_{ell}) < \epsilon$, which includes Huber contamination model as a special case. Therefore a (α, β) -GAN with suitable choice of network architecture, can robustly learn the generative model from arbitrary contamination Q when ϵ is small (e.g. no more than $1/3$).

In the current case, the denoising autoencoder network is modified to $G_\theta(y)$, providing us an universal approximation of the location (mean) of the inverse generative model as Eq. (7), where the noise can be any member of the elliptical distribution. Moreover, the discriminator is adapted to the image classification problem in the current case. Equipped with this design, the proposed (α, β) -GAN may help enhance the denoising Autoencoder robustness against unknown contamination, e.g. the Huber contamination model for real contamination in the image data. The experimental results in fact confirms the efficacy of such a design.

In addition, Wasserstein GAN (WGAN) is not a member of this β -GAN family. Compared to JS-GAN, WGAN aims to minimize the Wasserstein distance between the sample distribution and the generator distribution. Therefore, WGAN is not robust in the sense of contamination models above as arbitrary ϵ portion of outliers can be far away from the main distribution P_0 such that the Wasserstein distance is arbitrarily large.

Stablized Robust Denoising by Joint Autoencoder and β -GAN

Although β -GAN can robustly recover model parameters with contaminated samples, as a zero-sum game involving a non-convex-concave minimax optimization problem, training GANs is notoriously unstable with typical cyclic dynamics and possible mode collapse entrapped by local optima (Arjovsky et al. (2017)). However, in this section we show that the introduction of Autoencoder loss is able to

stabilize the training and avoid the mode collapse. In particular, Autoencoder can help stabilize GAN during training, without which the training processes of GAN are often oscillating and sometimes collapsed due to the presence of high noise.

Compared with the autoencoder, β -GAN can further help denoising by exploiting common information in similar samples during distribution training. In GAN, the divergence or Wasserstein distance between the reference image set and the denoised image set is minimized. The similar images can therefore help boost signals for each other.

For these considerations, a combined loss is proposed with both β -GAN and Autoencoder reconstruction loss,

$$\hat{\mathcal{L}}_{GAN}(x, \hat{x}) + \lambda \|x - \hat{x}\|_p^p, \quad (17)$$

where $p \in \{1, 2\}$ and $\lambda \geq 0$ is a trade-off parameter for ℓ_p reconstruction loss. Algorithm 1 summarizes the procedure of joint training of Autoencoder and GAN, which will be denoted as “GAN+ ℓ_p ” in the experimental section depending on the proper choice of GAN and p . The main algorithm is shown in Algorithm 1.

Algorithm 1 Joint training of (α, β) -GAN and ℓ_p -Autoencoder.

Input:

1. (α, β) for $S(t, 1) = -\int_t^1 c^{\alpha-1}(1-c)^\beta dc$, $S(t, 0) = -\int_0^t c^\alpha(1-c)^{\beta-1} dc$
or $S(t, 1) = t$, $S(t, 0) = -t$ for WGAN
 2. λ regularization parameter of the ℓ_p -Autoencoder
 3. k_d number of iterations for discriminator, k_g number of iterations for generator
 4. η_d learning rate of discriminator, η_g learning rate of generator
 5. ω weights of discriminator, θ weights of generator
 - 1: **for** number of training iterations **do**
 - 2: • Sample minibatch of m examples $\{(x^{(1)}, y^{(1)}), \dots, (x^{(m)}, y^{(m)})\}$ from reference-noisy image pairs.
 - 3: **for** $k = 1, 2, \dots, k_d$ **do**
 - 4: • Update the discriminator by gradient ascent:
 - 5: $g_\omega \leftarrow \frac{1}{m} \sum_{i=1}^m \nabla_\omega [S(D_\omega(x_i), 1) + S(D_\omega(G_\theta(y_i)), 0) + \mu(\|\nabla_{\tilde{x}} D_\omega(\tilde{x}_i)\|_2 - 1)^2]$
 where $\mu > 0$ for WGANgp only;
 - 6: $\omega \leftarrow \omega + \eta_d g_\omega$
 - 7: **end for**
 - 8: **for** $k = 1, 2, \dots, k_g$ **do**
 - 9: • Update the generator by gradient descent:
 - 10: $g_\theta \leftarrow \frac{1}{m} \sum_{i=1}^m \nabla_\theta [S(D_\omega(G_\theta(y_i)), 0) + \lambda |G_\theta(y_i) - x_i|^p]$, $p \in \{1, 2\}$;
 - 11: $\theta \leftarrow \theta - \eta_g g_\theta$
 - 12: **end for**
 - 13: **end for**
- Return:** Denoised image: $\hat{x}_i = G_\theta(y_i)$
-

Stability of combining Autoencoder into GAN

We illustrate that Autoencoder is indispensable to GANs in stabilizing the training in the joint training of Autoencoder and GAN scheme.

As an illustration, Fig. 2 shows the comparison of training a JS-GAN and a joint JS-GAN + ℓ_1 -Autoencoder. Training and test mean square error curves are plotted against iteration numbers in the RNAP data under $SNR = 0.1$ as Fig. 2. It shows that JS-GAN training suffers from drastic oscillations while joint training of JS-GAN + ℓ_1 -Autoencoder exhibits a stable process. In fact, with the aid of Autoencoder here, one does not need the popular “log D trick” in JS-GAN.

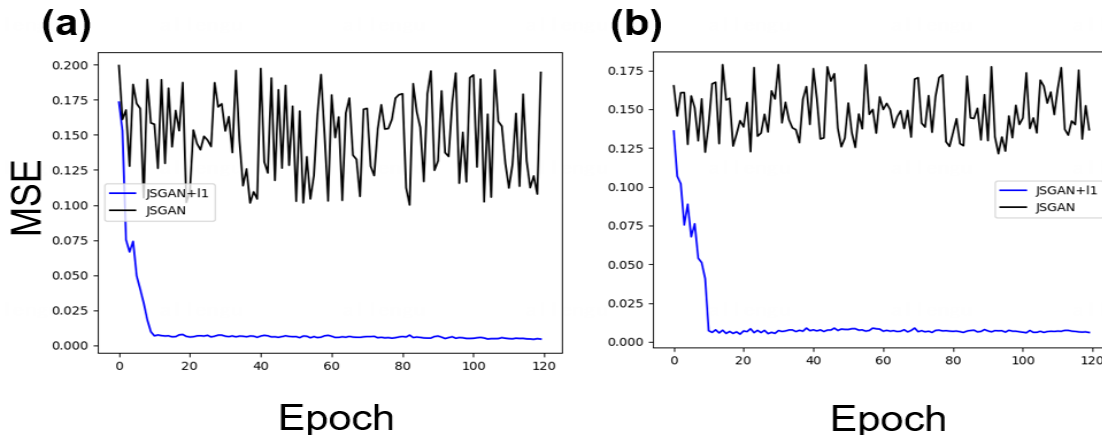


Fig. 2: Comparison between JS-GAN (black) and joint JS-GAN- ℓ_1 Autoencoder (blue). (a) and (b) are the change of MSE in training and testing data. Joint training of JS-GAN- ℓ_1 Autoencoder is much more stable than pure JS-GAN training that oscillates a lot.

Application: Robust Denoising of Cryo-EM Images

Datasets

RNAP: Simulation Dataset

We design a conformational heterogeneous dataset obtained by simulations. We use *Thermus aquaticus* RNA Polymerase (RNAP) in complex with σ^A factor (*Taq* holoenzyme) for our dataset. RNAP is the enzyme that transcribes RNA from DNA (transcription) in the cell. During the initiation of transcription, the holoenzyme must bind to the DNA, then separate the double-stranded DNA into single-stranded (Browning and Busby (2004)). *Taq* holoenzyme has a crab-claw like structure, with two flexible domains, the clamp and β pincers. The clamp, especially, has been suggested to play an important role in the initiation, as it has been captured in various conformations by CryoEM during initiation (Chen et al. (2020)). Thus, we focus on the movement of the clamp in this study. To generate the heterogeneous dataset, we start with two crystal structures of *Taq* holoenzyme, which vary in their clamp conformation, open (PDB ID: 1L9U (Murakami et al. (2002))) and closed (PDB ID: 4XLN (Bae et al. (2015))) clamp. For the closed clamp structure, we remove the DNA and RNA in the crystal structure, leaving only the RNAP and σ^A for our dataset. The *Taq* holoenzyme has about 370 kDa molecular weight. We then generate the clamp intermediate structures between the open and closed clamp using multiple-basin coarse-grained (CG) molecular dynamic (MD) simulations (Okazaki et al. (2006); Kenzaki et al. (2011)). CG-MD simulations simplify the system such that the atoms in each amino acid are represented by one particle. The structures from CG-MD simulations are refined back to all-atom or atomic structures using PD2 ca2main (Moore et al. (2013)) and SCRWL4 (Krivov et al. (2009)). Five structures with equally-spaced clamp opening angle are chosen for our heterogeneous dataset (shown in Fig. 3). Then, we convert the atomic structures to $128 \times 128 \times 128$ volumes using Xmipp package (Marabini et al. (1996)) and generate the 2D projections with an image size of 128×128 pixels. We further contaminate those clean images with additive Gaussian noise at different Signal-to-Noise Ratio (SNR): $SNR = 0.05$. The SNR is defined as the ratio of signal power and the noise power in the real space. For simplicity, we did not apply the contrast transfer function (CTF) to the datasets, and all the images are centered. Fig. 3 shows the five conformation pictures.

Training data size is 25000 paired images(noisy and reference images), Test data to calculate the MSE, PSNR and SSIM is another 1500 paired images.

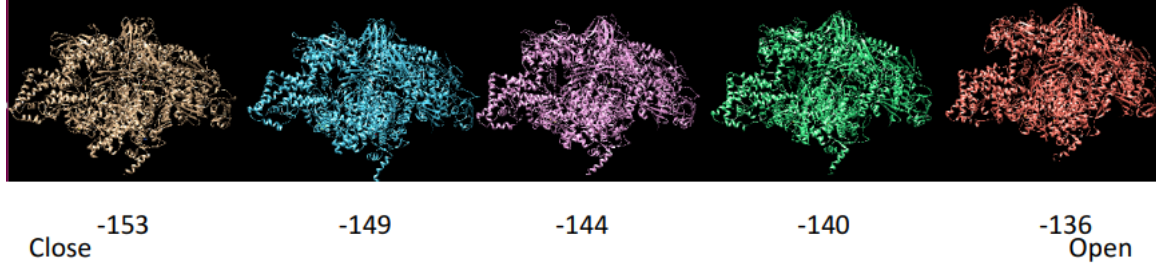


Fig. 3: Five conformations in RNAP heterogeneous dataset, from left to right are close conformation to open conformation of different angles.

EMPIAR-10028: Real Dataset

This is a real-world experimental dataset that was firstly studied in: the *Plasmodium falciparum* 80S ribosome dataset (EMPIAR-10028) (Wong et al. (2014)). They recover the Cryo-EM structure of the cytoplasmic ribosome from the human malaria parasite, *Plasmodium falciparum*, in complex with emetine, an anti-protozoan drug, at 3.2Å resolution. Ribosome is the essential enzyme that translates RNA to protein molecules, the second step of central dogma. The inhibition of ribosome activity of *Plasmodium falciparum* would effectively kill the parasite (Wong et al. (2014)). We can regard this dataset to have homogeneous property. This dataset contains 105247 noisy particles with an image size of 360×360 pixels. In order to decrease the complexity of the computing, we pick up the center square of each image with a size of 256×256 , since the surrounding area of the image is entirely useless that does not lose information in such a preprocessing. Then the 256×256 images are fed as the input of the G_θ -network (Fig. 4). Since the GAN-based method needs clean images as reference, we prepare their clean counterparts in the following way: we first use cryoSPARC1.0 (Punjani et al. (2017)) to build a 3.2Å resolution volume and then rotate the 3D-volume by the Euler angles obtained by cryoSPARC to get projected 2D-images. The training data size we pick is 19500, and the test data size is 500.

Evaluation Method

We exploit the following three metrics to determine whether the denoising result is good or not. They are the Mean Square Error (MSE), the Peak Signal-to-Noise Ratio (PSNR) and the Structural Similarity Index Measure (SSIM).

- **(MSE)** For images of size $d_1 \times d_2$, the Mean Square Error (MSE) between the reference image x and the denoised image \hat{x} is defined as,

$$\text{MSE} := \frac{1}{d_1 d_2} \sum_{i=1}^{d_1} \sum_{j=1}^{d_2} (x(i, j) - \hat{x}(i, j))^2.$$

The smaller is the MSE, the better the denoising result is.

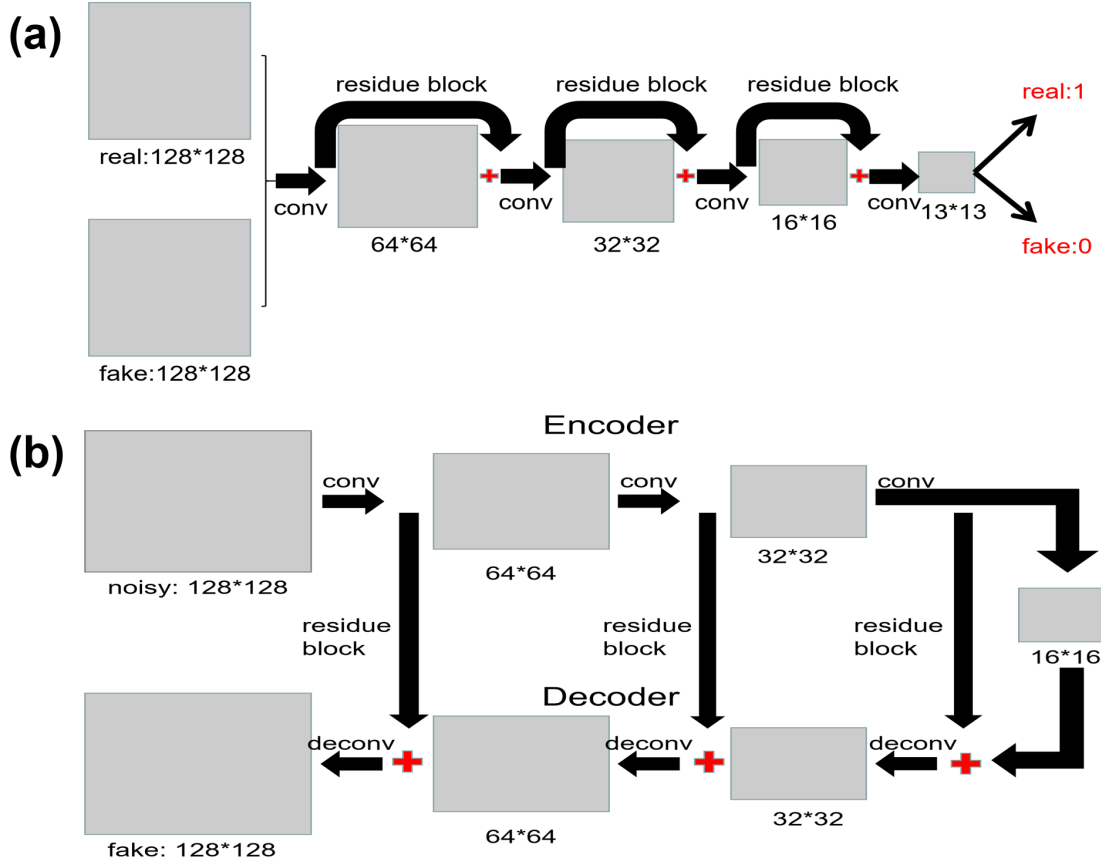


Fig. 4: The architectures of (a) discriminator D and (b) generator G , which borrow the residue structure. The input image size (128×128) here is adapted to RNAP dataset, while input image size of EMPIAR-10028 dataset is 256×256 .

- **(PSNR)** Similarly, the Peak Signal-to-Noise Ratio (PSNR) between the reference image x and the denoised image \hat{x} whose pixel value range is $[0, t]$ (1 by default), is defined by

$$\text{PSNR} := 10 \log_{10} \frac{t^2}{\frac{1}{d_1 d_2} \sum_{i=1}^{d_1} \sum_{j=1}^{d_2} (x(i, j) - \hat{x}(i, j))^2}.$$

The larger is the PSNR, the better the denoising result is.

- **(SSIM)** The third criterion is the Structural Similarity Index Measure (SSIM) between reference image x and denoised image \hat{x} is defined in Wang et al. (2004),

$$\text{SSIM} = \frac{(2\mu_x \mu_{\hat{x}} + c_1)(2\sigma_x \sigma_{\hat{x}} + c_2)(\sigma_{x\hat{x}} + c_3)}{(\mu_x^2 + \mu_{\hat{x}}^2 + c_1)(\sigma_x^2 + \sigma_{\hat{x}}^2 + c_2)(\sigma_x \sigma_{\hat{x}} + c_3)}.$$

where μ_x ($\mu_{\hat{x}}$) and σ_x ($\sigma_{\hat{x}}$) are the mean and variance of x (\hat{x}), respectively, $\sigma_{x\hat{x}}$ is covariance of x and \hat{x} , $c_1 = K_1 L^2$, $c_2 = K_2 L^2$, $c_3 = \frac{c_2}{2}$ three variables to stabilize the division with weak denominator ($K_1 = 0.01$, $K_2 = 0.03$ by default), L is the dynamic range of the pixel-value (1 by default). The value SSIM of lies in $[0, 1]$, where the closer it is to 1, the better the result is.

Although these metrics are widely used in image denoising, they might not be the best metrics for Cryo-EM images. In Appendix “**Influence of the regularization parameter: λ** ”, it shows an example that the best-reconstructed images perhaps do not meet the best MSE/PSNR/SSIM metrics.

In addition to these metrics, we consider the 3D reconstruction based on denoised images. Particularly, we take the 3D reconstruction by RELION to validate the denoised result. The procedure of our RELION reconstruction is follows: firstly creating the 3D initial model, then doing 3D classification, followed by operating 3D auto-refine. Moreover, for heterogeneous conformations in simulation data, we further turn the denoising results into a clustering problem to measure the efficacy of denoising methods, whose details will be discussed in Appendix “[Clustering to solve the conformational heterogeneity](#)”.

Network Architecture and Hyperparameter

In the experiments of this chapter, the best results come from the ResNet architecture (Su et al. (2018)) shown in Fig. 4, which has been successfully applied to study biological problems such as predicting protein-RNA binding. The generator in such GANs exploits the Autoencoder network architecture, while the discriminator is a binary classification ResNet. In Appendix “[Convolution network](#)” and “[Test RNAP dataset with PGGAN strategy](#)”, we also discuss a Convolutional Network without residual blocks and the PGGAN (Karras et al. (2018)) strategy with their experimental results, respectively.

We chose Adam (Kingma and Ba (2015)) for the Optimization. The learning rate of the discriminator is $\eta_d = 0.001$, and the learning rate of the generator is $\eta_g = 0.01$. We choose $m = 20$ as our batch size, $k_d = 1$, and $k_g = 2$ in Algorithm 1.

For (α, β) -GAN, we reports two types of choices: (1) $\alpha = 1, \beta = 1$; (2) $\alpha = 0.5, \beta = 0.5$ since they show the best results in our experiments, while the others are collected in Appendix “[Influence of parameter \$\(\alpha, \beta\)\$ brings in \$\beta\$ -GAN](#)”. For WGAN, the gradient penalty with parameter $\mu = 10$ is used to accelerate the speed of convergence and hence the algorithm is denoted as WGANgp below. The trade-off (regularization) parameter of ℓ_1 or ℓ_2 reconstruction loss is set to be $\lambda = 10$ through out this section, while an ablation study on varying λ is discussed in Appendix “[Influence of the regularization parameter: \$\lambda\$](#) ”.

Results for RNAP

Denoising without contamination

In this part, we attempt to denoise the noisy image without the contamination (i.e., $\epsilon = 0$ in Eq. (8)). In order to present the advantage of GAN, we compare the denoising result in different methods. Table 1 shows the MSE and PSNR of different methods in SNR 0.05 and 0.1. We recognize the traditional methods such as KSVD, BM3D, Non-local mean, and CWF can remove the noise partially and extract the general outline, but they still leave the unclear piece. However, deep learning methods can perform much better. Specifically, we observe that GAN-based methods, especially WGANgp + ℓ_1 loss and (.5, .5)-GAN + ℓ_1 loss, perform better than denoising Autoencoder methods, which only optimizes ℓ_1 or ℓ_2 loss. The adversarial process inspires the generation process, and the additional ℓ_1 loss optimization speeds up the process of generation towards reference images. Notably, WGANgp and (5, .5)- or (1, 1)-GANs are among the best methods, where the best mean performance up to one standard deviation are all marked in bold font. Specifically, compared with (.5, .5)-GAN, the WGANgp get better PSNR and SSIM in SNR 0.1; the (.5, .5)-GAN shows the advantage in PSNR and SSIM in SNR 0.05 while (1, 1)-GAN is competitive within one standard deviation. Also, Fig. 5(a) presents the denoised images of denoising methods in SNR 0.05. For the convenience of comparison, we choose a clear open-conformation (the rightmost conformation of Fig. 3) to present, and the performances show that WGANgp and (α, β) -GAN can grasp the “open” shape completely and derive the more explicit pictures than other methods.

Table 1: Denoising result without contamination in simulated RNAP dataset: MSE, PSNR and SSIM of different models, such as BM3D (Dabov et al. (2007)), KSVD (Aharon et al. (2006)), Non-local means (Wei and Yin (2010)), CWF (Bhamre et al. (2016)), DA and GAN-based methods.

Method/SNR	MSE		PSNR		SSIM	
	0.1	0.05	0.1	0.05	0.1	0.05
BM3D	3.52e-2 (7.81e-3)	5.87e-2(9.91e-3)	14.54(0.15)	12.13(0.14)	0.20(0.01)	0.08(0.01)
KSVD	1.84e-2(6.58e-3)	3.49e-2(7.62e-3)	17.57(0.16)	14.61(0.14)	0.33(0.01)	0.19(0.01)
Non-local means	5.02e-2(5.51e-3)	5.81e-2(8.94e-3)	13.04(0.50)	12.40(0.65)	0.18(0.01)	0.09(0.01)
CWF	2.53e-2(2.03e-3)	9.28e-3(8.81e-4)	16.06(0.33)	20.31(0.41)	0.25(0.01)	0.08(0.01)
ℓ_2 -Autoencoder ²	3.13e-3(7.97e-5)	4.02e-3(1.48e-4)	25.10(0.11)	23.67(0.77)	0.79(0.02)	0.79(0.01)
ℓ_1 -Autoencoder ³	3.16e-3(7.05e-5)	4.23e-3(1.32e-4)	25.05(0.09)	23.80(0.13)	0.77(0.02)	0.76(0.01)
(0, 0)-GAN + ℓ_1 ⁴	3.06e-3(5.76e-5)	4.02e-3(5.67e-4)	25.25(0.04)	24.00(0.06)	0.78(0.03)	0.78(0.03)
WGANgp + ℓ_1	2.95e-3(1.41e-5)	4.00e-3(8.12e-5)	25.42(0.04)	24.06(0.05)	0.83(0.02)	0.80(0.03)
(1, 1)-GAN + ℓ_1	2.99e-3(3.51e-5)	4.01e-3(1.54e-4)	25.30(0.05)	24.07(0.16)	0.82(0.03)	0.79(0.03)
(.5, .5)-GAN+ ℓ_1	3.01e-3(2.81e-5)	3.98e-3(4.60e-5)	25.27(0.04)	24.07(0.05)	0.79(0.04)	0.80(0.03)

What’s more, in order to test the denoised results of β -GAN, we reconstruct the 3D volume by RELION in 200000 images of SNR 0.1, which are denoised by (.5, .5)-GAN + ℓ_1 . The value of pixel size, amplitude contrast, spherical aberration and voltage are 1.6, 2.26, 0.1 and 300. For the other terms, retaining the default settings in RELION software. Fig. 5(b) and (c) separately show the 3D volume recovered by clean images and denoised images. Also, the related FSC curves are shown in Fig. 5(d). Specifically, the blue curve, which represents the denoised images in (.5, .5)-GAN + ℓ_1 is closed to red curves representing the clean images. We use the 0.143 cutoff criterion in literature (the resolution as Fourier shell correlation reaches 0.143, shown by dash lines in Fig. 5(d)) to choose the final resolution: 3.39Å. The structure recovered by (.5, .5)-GAN + ℓ_1 and FSC curve are as good as the original structure, which illustrates that the denoised result of β -GAN can identify the details of image and be helpful in 3D reconstruction.

In addition, Appendix “Clustering to solve the conformational heterogeneity” also shows an example that GAN with ℓ_1 -Autoencoder helps heterogeneous conformation clustering.

Robustness under contamination

We also consider the contamination model $\epsilon \neq 0$ and Q from purely noisy images. We randomly replace partial samples of our training dataset of RNAP by noise to test whether our model is robust or not. There are three types to test: (A) Only replacing the clean reference images. It implies the reference images are wrong or missing, such that we do not have the reference images to compare. This is the worst contamination case. (B) Only replacing the noisy images. It means the Cryo-EM images which the machine produces are broken. (C) Replacing both, which indicates both A and B happen. The latter two are mild contamination cases, especially C that replaces both reference and noisy images by Gaussian noise whose ℓ_1 or ℓ_2 loss is thus well-controlled.

Here we test our robustness of various deep learning based methods using the RNAP data of SNR 0.1, and the former three types of contamination is applied to randomly replace the samples in the proportion of $\epsilon \in \{0.1, 0.2, 0.3\}$ of the whole dataset.

Fig. 5(e), (f) and (g) compare the robustness of different methods. In all the cases, some β -GANs ((.5, .5)- and (1, 1)-) with ℓ_1 -Autoencoder exhibit relatively universal robustness. Particularly, (1) The MSE with ℓ_1 loss is less than the MSE with ℓ_2 loss, which represents the ℓ_1 loss is more robust than ℓ_2 as desired. (2) The Autoencoder method in ℓ_2 loss and WGANgp show certain robustness in case B and C but are largely influenced by contamination in case A (shown in Figure 5 (e)), indicating the most serious damage arising from type A, merely replacing only the reference image by Gaussian noise. The

² ℓ_2 -Autoencoder represents ℓ_2 loss

³ ℓ_1 -Autoencoder represents ℓ_1 loss

⁴ GAN + ℓ_1 represents adding ℓ_1 regularization in GAN generator loss

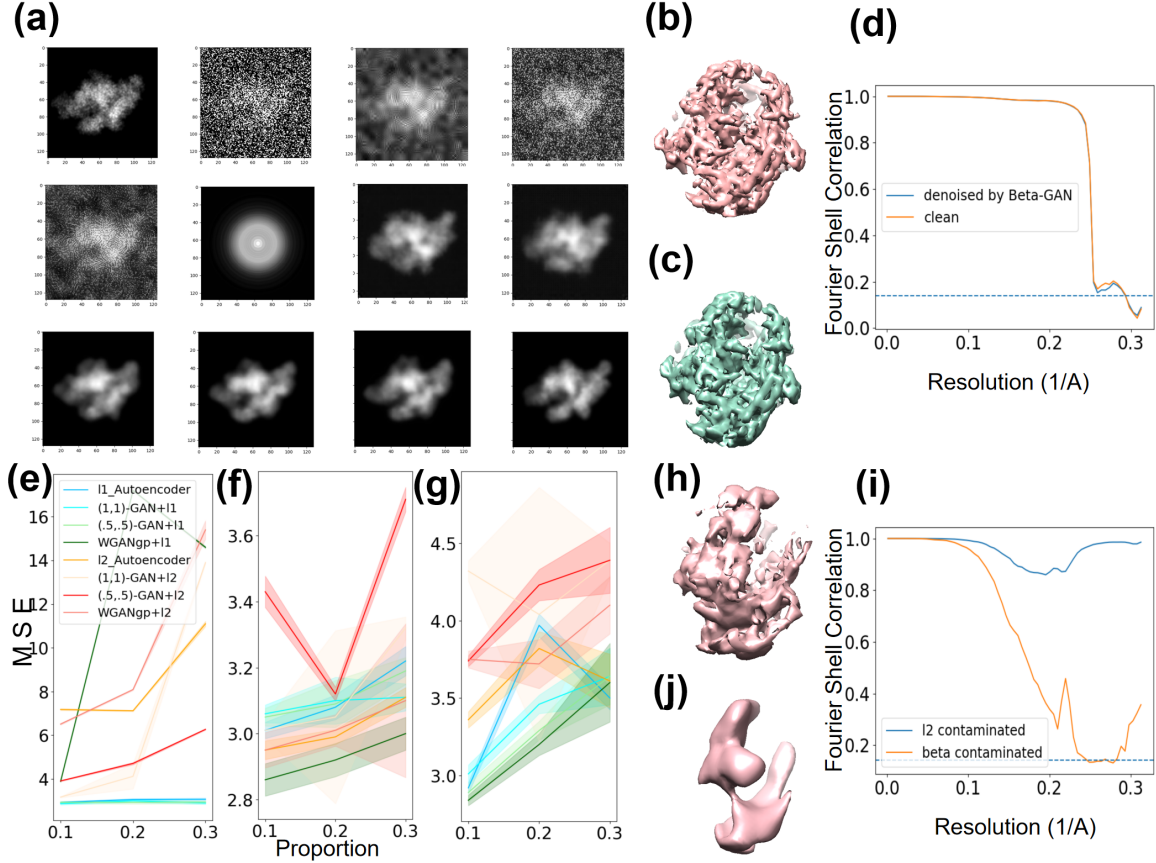


Fig. 5: Results for RNAP dataset. (a) is denoised images in different denoised methods (from left to right, top to bottom): Clean, Noisy, BM3D, KSVD, Non-local means, CWF, ℓ_1 -Autoencoder, ℓ_2 -Autoencoder, (1,1)-GAN + ℓ_1 , (0,0)-GAN + ℓ_1 , (.5,.5)-GAN + ℓ_1 and WGANgp + ℓ_1 . (b) and (c) are reconstruction of clean images and (.5,.5)-GAN + ℓ_1 denoised images. (d) is FSC curve of (b) and (c). (e), (f) and (g) are robustness tests of various methods under $\epsilon \in \{0.1, 0.2, 0.3\}$ -proportion contamination in three types of contamination: (e) Type A: replacing the reference images with random noise; (f) Type B: replacing the noisy images with random noise; (g) Type C: replacing both with random noise. (h) and (j) are reconstructions of images with (.5,.5)-GAN + ℓ_1 and ℓ_2 -Autoencoder under type A contamination, respectively, where ℓ_2 -Autoencoder totally fails but (.5,.5)-GAN + ℓ_1 is robust. (i) shows FSC curves of (h) and (j).

reason is that the ℓ_2 Autoencoder and WGANgp method are confused by the wrong reference images so that they can not learn the mapping from data distribution to reference distribution accurately. (3) In the type C, the standard deviations of the five best models are larger compared the other two types. The contamination of both noisy y and clean x images influence the the stability of model more than the other two types.

Furthermore, we take an example in type A contamination with $\epsilon = 0.1$ for 3D reconstruction. The 3D reconstruction in denoised images with (.5,.5)-GAN + ℓ_1 and ℓ_2 -Autoencoder are shown in Fig. 5(h) and (j), and related FSC curve is Fig. 5(i). Specifically, on the one hand, the blue FSC curve of ℓ_2 -Autoencoder doesn't drop, which leads to the worse reconstruction; on the other hand, the red FSC curve of (.5,.5)-GAN + ℓ_1 drops quickly but begins to rise again, whose reason is that some unclear detail of structure mixed angular information in reconstruction. When applying 0.143 cutoff criterion (dashed line in FSC curve), the resolution of (.5,.5)-GAN + ℓ_1 is about 4Å. Although

reconstruction of images and final resolution is not better than the clean images, it is much clearer than ℓ_2 -Autoencoder which totally fails in the contamination case. The outcome of the reconstruction demonstrates that $(.5, .5)$ -GAN + ℓ_1 is relatively robust, whose 3D result is consistent with the clean image reconstruction.

In summary, some (α, β) -GANs methods, such as the $(.5, .5)$ -GAN and $(1, 1)$ -GAN, with ℓ_1 -Autoencoder are more resistant to sample contamination, which are better to be applied into the denoising of Cryo-EM data.

Results for EMPIAR-10028

The following Fig. 6(a) and (b) show the denoising results by different deep learning methods in experimental data: ℓ_1 or ℓ_2 Autoencoders, JS-GAN ($(0, 0)$ -GAN), WGANp, and (α, β) -GAN, where we add ℓ_1 loss in all of the GAN-based structures. Although the Autoencoder can grasp the shape of macromolecules, it is a little blur in some parts. What is more, WGANp and $(.5, .5)$ -GAN perform better than other deep learning methods according to MSE and PSNR, which is largely consistent with the result of the RNAP dataset. The improvements of such GANs over pure Autoencoders lie in their ability of utilizing structural information among similar images to learn the data distribution better.

Finally, we implement reconstruction via RELION of 100000 images, which denoised by $(.5, .5)$ -GAN + ℓ_1 . The parameters are the same as the ones set in the paper (Wong et al. (2014)). The reconstruction results are shown in Fig. 6(c). It is demonstrated that the final resolution is 3.20\AA , which is derived by FSC curve in Fig. 6(d) using the same 0.143 cutoff (dashed line) to choose the final resolution. We note that the final resolution by RELION after denoising is as good as the original resolution 3.20\AA reported in Wong et al. (2014).

Conclusion and Discussion

In this chapter, we set a connection between the traditional image forward model and Huber contamination model in solving the complex contamination in the Cryo-EM dataset. The joint training of Autoencoder and GAN has been proved to substantially improve the performance in Cryo-EM image denoising. In this joint training scheme, the reconstruction loss of Autoencoder helps GAN to avoid mode collapse and stabilize training. GAN further helps Autoencoder in denoising by utilizing the highly correlated Cryo-EM images since they are 2D projections of one or a few 3D molecular conformations. To overcome the low Signal-to-Noise Ratio challenge in Cryo-EM images, joint training of ℓ_1 -Autoencoder combined with $(.5, .5)$ -GAN, $(1, 1)$ -GAN, and WGAN with gradient penalty is often among the best performance in terms of MSE, PSNR, and SSIM when the data is contamination-free. However, when a portion of data is contaminated, especially when the reference data is contaminated, WGAN with ℓ_1 -Autoencoder may suffer from the significant deterioration of reconstruction accuracy. Therefore, robust ℓ_1 Autoencoder combined with robust GANs ($(.5, .5)$ -GAN and $(1, 1)$ -GAN) are the overall best choices for robust denoising with contaminated and high noise datasets.

Part of the results in this chapter is based on a technical report (Gu et al. (2020)). Most of the deep learning-based techniques in image denoising need reference data, limiting themselves in the application of Cryo-EM denoising. For example, in our experimental dataset EMPIAR-10028, the reference data is generated by the cryoSPARC, which itself becomes problematic in highly heterogeneous conformations. Therefore, the reference image we learn may follow a fake distribution. How to denoise without the reference image thus becomes a significant problem. It is still open how to adapt to different experiments and those without reference images. In order to overcome this drawback, an idea called "image-blind denoising" was offered by the literature (Lehtinen et al. (2018); Krull et al. (2019)), which viewed the noisy image or void image as the reference image to denoise. Besides, Chen et al. (2018) tried to extract the noise distribution from the noisy image and gain denoised images

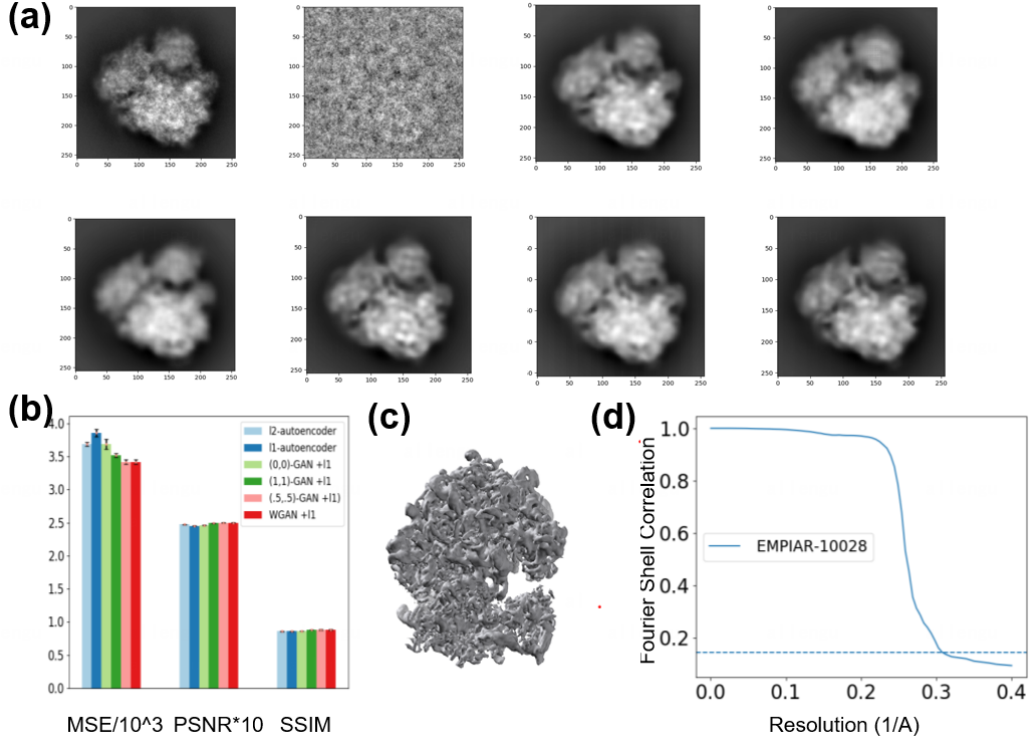


Fig. 6: Results for EMPIAR-10028. (a) Comparison in EMPIAR-10028 dataset in different deep learning methods (from left to right, top to bottom): clean image, noisy image, ℓ_1 -Autoencoder, ℓ_2 -Autoencoder, (0,0)-GAN + ℓ_1 , (1,1)-GAN + ℓ_1 , (.5,.5)-GAN + ℓ_1 , WGANgp + ℓ_1 . (b) is the MSE, PSNR and SSIM in different denoised methods. (c) and (d) are the 3D-reconstruction of denoised images by (.5,.5)-GAN + ℓ_1 and the FSC curve, respectively. The resolution of reconstruction from (.5,.5)-GAN + ℓ_1 denoised images is 3.20Å, which is as good as the original resolution.

through removing the noise for noisy data; [Quan et al. \(2020\)](#) augmented the data by Bernoulli sampling and denoise image with dropout. Nevertheless, all of the methods need noise is independent of the elements themselves. Thus it is hard to remove noise in Cryo-EM because the noise from ice and machine is related to the particles.

In addition, for reconstruction problems in Cryo-EM, [Zhong et al. \(2020\)](#) proposed an end-to-end 3D reconstruction approach based on the network from Cryo-EM images, where they attempt to borrow the Variational Autoencoder (VAE) to approximate the forward reconstruction model and recover the 3D structure directly by combining the angle information and image information learned from data. This is one future direction to pursue.

Appendix

Influence of parameter (α, β) brings in β -GAN

In this part, we have applied β -GAN into denoising problem. How to pick up a good parameter: (α, β) in the β -GAN becomes an important issue. Therefore, we investigate the impact of the parameter (α, β) on the outcome of denoising. We choose eight significant groups of α, β . Our result is shown in

Table 2. It is demonstrated that the effect of these groups in different parameters is not large. The best result appears in $\alpha = 1, \beta = 1$ and $\alpha = 0.5, \beta = 0.5$

Table 2: The result of β -GANs with ResNet architecture: MSE, PSNR and SSIM of different (α, β) in β -GAN under various levels of Gaussian noise corruption in RNAP dataset.

Parameter/SNR	MSE		PSNR		SSIM	
	0.1	0.05	0.1	0.05	0.1	0.05
$\alpha = 1, \beta = 1$	2.99e-3(3.51e-5)	4.01e-3(1.54e-4)	25.30(0.05)	24.07(0.16)	0.82(0.03)	0.79(0.03)
$\alpha = 0.5, \beta = 0.5$	3.01e-3(2.81e-5)	3.98e-3(4.60e-5)	25.27(0.04)	24.07(0.05)	0.79(0.04)	0.80(0.03)
$\alpha = -0.5, \beta = -0.5$	3.02e-3(1.69e-5)	4.15e-3(5.05e-5)	25.27(0.02)	23.91(0.05)	0.80(0.03)	0.80(0.03)
$\alpha = -1, \beta = -1$	3.05e-3(3.54e-5)	4.12e-3(8.30e-5)	25.23(0.05)	23.93(0.08)	0.80(0.05)	0.77(0.04)
$\alpha = 1, \beta = -1$	3.05e-3(4.30e-5)	4.10e-3(5.80e-5)	25.24(0.06)	23.96(0.06)	0.82(0.02)	0.76(0.03)
$\alpha = 0.5, \beta = -0.5$	3.09e-3(6.79e-5)	4.05e-3(6.10e-5)	25.17(0.04)	24.01(0.06)	0.79(0.04)	0.77(0.05)
$\alpha = 0, \beta = 0$	3.06e-3(5.76e-5)	4.02e-3(5.67e-4)	25.23(0.04)	24.00(0.06)	0.78(0.03)	0.78(0.03)
$\alpha = 0.1, \beta = -0.1$	3.07e-3(5.62e-5)	4.05e-3(8.55e-5)	25.23(0.08)	23.98(0.04)	0.78(0.02)	0.79(0.03)

Clustering to solve the conformational heterogeneity

In this part, we try to analyze whether the denoised result is good in solving conformation heterogeneity in simulated RNAP dataset. Specifically, for heterogeneous conformations in simulation data, we mainly choose the following two typical conformations: *open* and *close* conformations (the leftmost and rightmost conformations in Fig. 3) as our testing data. Our goal is to distinguish these two classes of conformations. However, different from the paper (Xian et al. (2018)), we do not have the template images to calculate the distance matrix, so what we try is unsupervised learning – clustering. Our clustering method is firstly using manifold learning: Isomap (Tenenbaum et al. (2000)) to reduce the dimension of the denoised images, then make use of k -Means ($k = 2$) to group the different conformations.

The Fig. 7(a) displays the 2D visualizations of two conformations about the clustering effect in different denoised methods. Here the SNR of noisy data is 0.05. In correspondence to those visualizations, the accuracy of competitive methods is reported: (1, 1)-GAN+ ℓ_1 : 54/60 (54 clustering correctly in 60), WGANgp+ ℓ_1 : 54/60, ℓ_2 -Autoencoder: 44/60, BM3D: 34/60, and KSVD: 36/60. This result shows that: clean images separate well; (α, β) -GAN and WGANgp with ℓ_1 Autoencoder can distinguish the open and close structure partially, although there exists several wrong points; ℓ_2 -Autoencoder and traditional techniques have poor performance because it is hard to detect the clamp shape.

Furthermore, the reason we use Isomap is it performs the best in our case and comparisons of different manifold learning methods are shown in Fig. 7(b). It demonstrates that blue and red points separate most in the graph of ISOMAP. Specifically, the accuracy of these four methods are 50/60 (spectral method), 46/50 (MDS), 46/50 (TSNE), and 54/60 (ISOMAP). it shown that Isomap can distinguish best in the two structures' images compared to other methods: such as the Spectral method (Ng et al. (2002)), MDS (Cox and Cox (2008)), and TSNE (Maaten and Hinton (2008)).

Convolution network

We present the result of simple deep convolution network (remove the ResNet block), the performances in all of criterion are worse than performances of the residue's architecture work. Table 3 compares the MSE and PSNR performance of various methods in the RNAP dataset with SNR 0.1 and 0.05. And Fig. 8(a) displays the denoised image of different methods in the RNAP dataset with SNR 0.05. It shows the advantage of residue structure in our GAN-based denoising Cryo-EM problem.

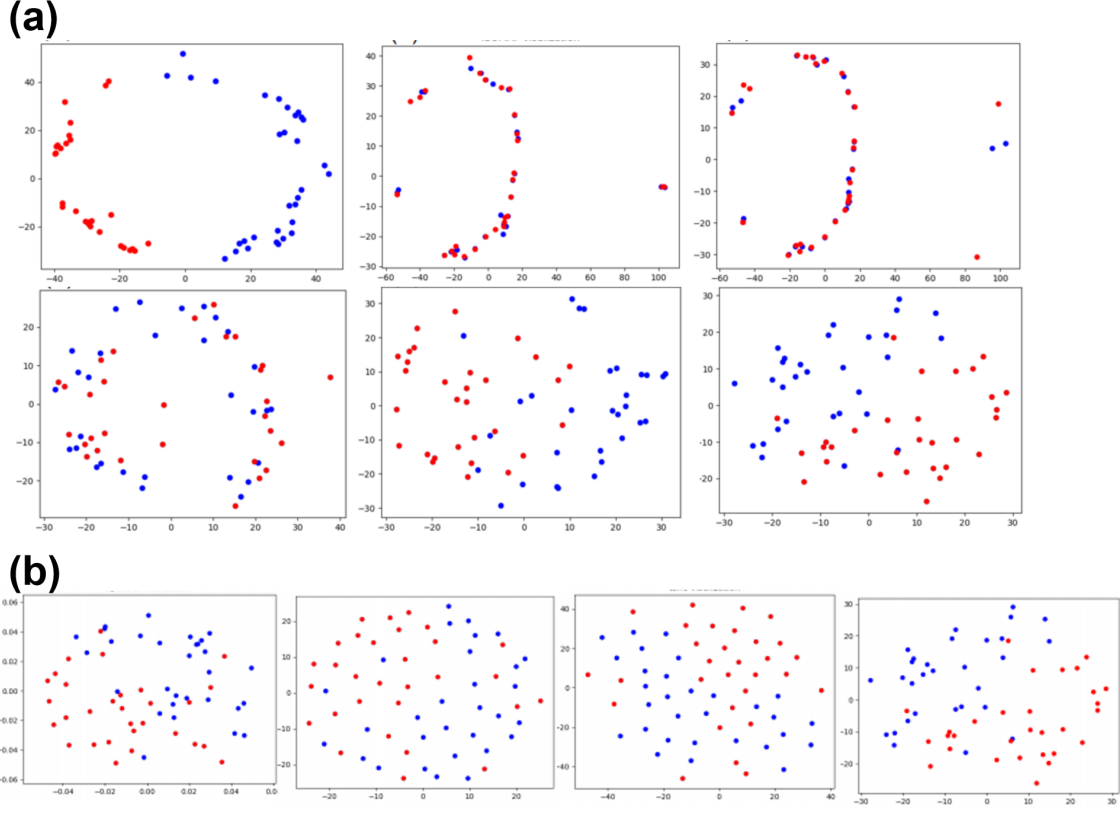


Fig. 7: 2D visualization of 2-conformational images in manifold learning. Red point, blue point separately represent the open and closed conformation. (a) is 2D visualization of 2-conformation image by ISOMAP in different methods (from the left and top to the right and bottom): clean image, BM3D, KSVD, ℓ_2 -Autoencoder, (1,1)-GAN+ ℓ_1 , WGANgp+ ℓ_1 . (b) is 2D visualization of 2-conformation image in different manifold learning methods (from left to right): Spectral methods, MDS, TSNE, and ISOMAP.

Table 3: MSE and PSNR of different models under various levels of Gaussian noise corruption in RNAP dataset, where the architecture of GANs or Autoencoders are simply convolution network.

Method/SNR	MSE		PSNR	
	0.1	0.05	0.1	0.05
BM3D	3.5e-2(7.8e-3)	5.9e-2(9.9e-3)	14.535(0.1452)	12.134(0.1369)
KSVD	1.8e-2(6.6e-3)	3.5e-2(7.6e-3)	17.570(0.1578)	14.609(0.1414)
Non-local means	5.0e-2(5.5e-3)	5.8e-2(8.9e-3)	13.040(0.4935)	12.404(0.6498)
CWF	2.5e-2(2.0e-3)	9.3e-3(8.8e-4)	16.059(0.3253)	20.314(0.4129)
ℓ_2 -Autoencoder	4.0e-3(6.0e-4)	6.7e-3(9.0e-4)	24.202(0.6414)	21.739(0.7219)
(0,0)-GAN + ℓ_1	3.8e-3(6.0e-4)	5.6e-3(8.0e-4)	24.265(0.6537)	22.594(0.6314)
WGANgp+ ℓ_1	3.1e-3(5.0e-4)	5.0e-3(8.0e-4)	25.086(0.6458)	23.010(0.6977)
(1,-1)-GAN + ℓ_1	3.4e-3(5.0e-4)	4.9e-3(9.0e-4)	24.748(0.7233)	23.116(0.7399)
(.5,-.5)-GAN + ℓ_1	3.5e-3(5.0e-4)	5.6e-3(9.0e-4)	24.556(0.6272)	22.575(0.6441)

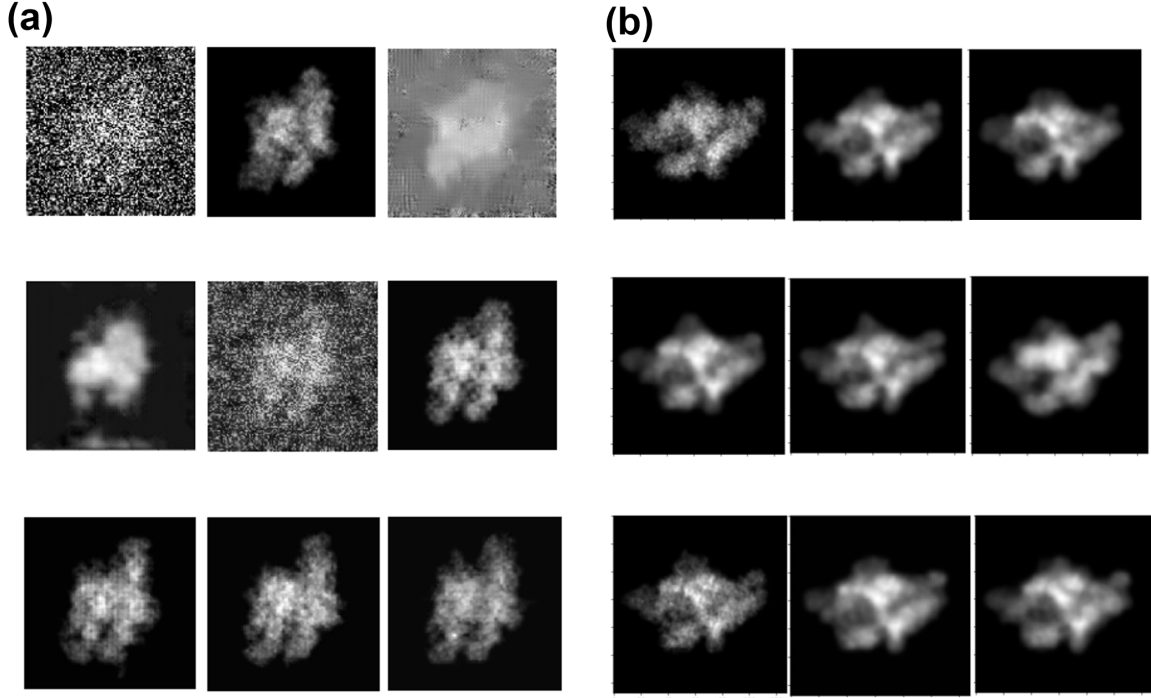


Fig. 8: (a) Denoised images with convolution network without ResNet structure in different methods in RNAP dataset with SNR 0.05 (from left to right, top to bottom): clean, noisy, BM3D, ℓ_2 -Autoencoder, KSVD, JS-GAN + ℓ_1 , WGANgp + ℓ_1 , $(1, -1)$ -GAN + ℓ_1 , $(.5, -.5)$ -GAN + ℓ_1 . (b) Denoised and reference images in different regularization λ (we use $(.5, .5)$ -GAN + $\lambda \ell_1$ as an example) in corresponding to Table 4. From left to right, top to bottom, the image is: Clean image, $\lambda = 0.1$, $\lambda = 1$, $\lambda = 5$, $\lambda = 10$, $\lambda = 50$, $\lambda = 100$, $\lambda = 500$, $\lambda = 10000$

Test RNAP dataset with PGGAN strategy

PGGAN (Karras et al. (2018)) is a popular method to generate high-resolution images from low resolution ones by gradually adding layers of generator and discriminator. It accelerates and stabilizes the model training. Since Cryo-EM images are in large pixel size that fits well the PGGAN method, here we choose its structure⁵ instead of the ResNet and convolution structures above to denoise Cryo-EM images. Our experiments partially demonstrate two things: 1) the denoised images sharpen more, though the MSE changes to be higher. 2) we do not need to add ℓ_1 regularization to make model training stable; it can also detect the outlier of images for both real and simulated data without regularization.

In detail, based on the PGGAN architecture and parameters, we test the following two objective functions developed in the section “**Robust Denoising Method**”: WGANgp and WGANgp + ℓ_1 , in the RNAP simulated dataset with SNR 0.05 as an example to explain. The denoised images are presented in Fig. 9; it is noted that the model is hard to collapse regardless of adding ℓ_1 regularization. The MSE of adding regularization is $8.09e-3(1.46e-3)$, which is less than $1.01e-2(1.81e-3)$ without adding regularization. Nevertheless, both of them don’t exceed the results based on the ResNet structure above. This shows that PGGAN architecture does not have more power than the ResNet structure. But an advantage of PGGAN lies in its efficiency in training. So it is an interesting problem to improve PGGAN toward the accuracy of ResNet structure.

⁵ We set the same architecture and parameters as <https://github.com/nashory/pggan-pytorch> and the input image size is 128×128 .

Another thing that needs to highlight is MSE may not be a good criterion because denoised images by PGGAN are clearer in some details than the front methods we propose. This phenomenon is also shown in Appendix “**Influence of the regularization parameter: λ** ”. So how to find a better criterion to evaluate the model and combine two strengths of ResNet-GAN and PGGAN await us to explore.

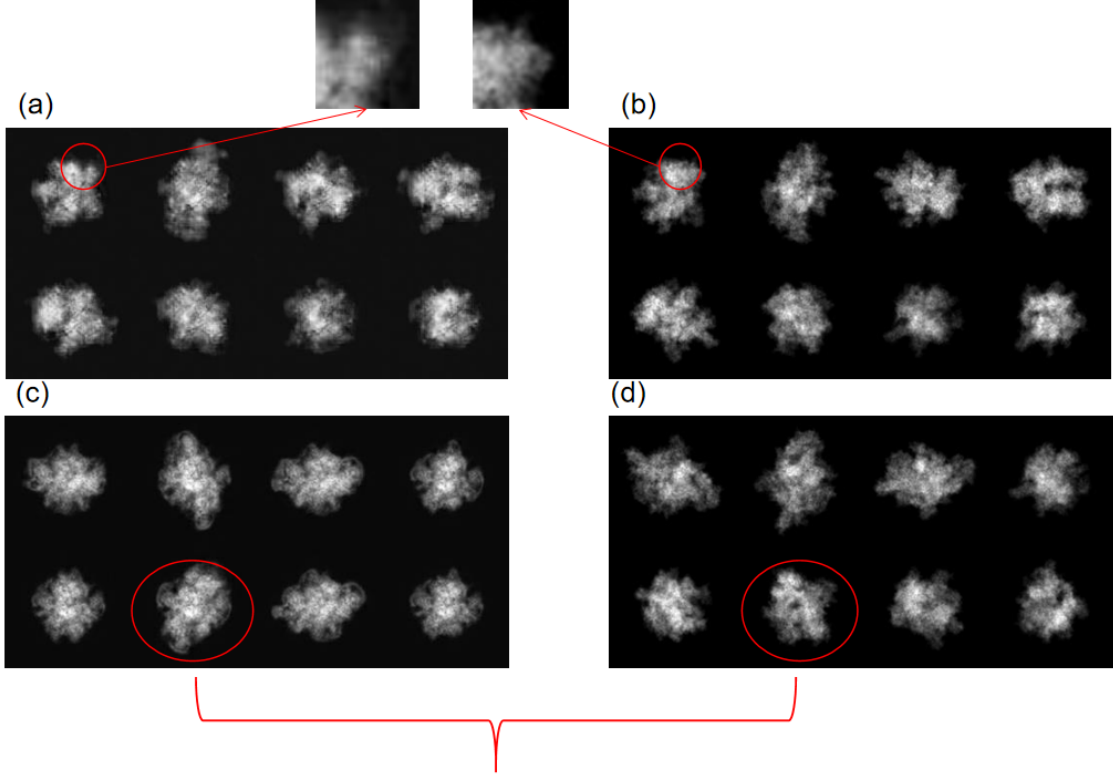


Fig. 9: Denoised and reference images by PGGAN instead of simple ResNet and Convolution structure in RNAP dataset with SNR 0.05. The PGGAN strategy is tested in two objective functions: WGANgp + ℓ_1 and WGANgp. (a) and (b) are denoised and reference images using PGGAN with WGANgp + ℓ_1 ; (c) and (d) are denoised and reference images using PGGAN in WGANgp, respectively. Specifically, the images highlighted in red color show the structural difference between denoised images and reference images. It demonstrates that denoised images are different from reference images using PGGAN strategy.

Influence of the regularization parameter: λ

In this chapter, we add ℓ_1 regularization to make model stable, but how to choose λ of ℓ_1 regularization becomes a significant problem. Here we take (.5, .5)-GAN to denoise in RNAP dataset with SNR 0.1. According to some results in different λ in Table 4, we find as the λ tends to infinity, the MSE results tends to ℓ_1 -Autoencoder, which is reasonable. Also, the MSE result becomes the smallest as the $\lambda = 10$.

What’s more, an interesting phenomenon is found that a much clearer result could be obtained at $\lambda = 100$ than that at $\lambda = 10$, although the MSE is not the best (shown in the Fig. 8(b)).

Table 4: MSE, PSNR and SSIM of different λ in (.5,.5)-GAN + λ_1 in RNAP dataset.

λ /criterion	MSE	PSNR	SSIM
0.1	3.06e-3(4.50e-5)	25.22(0.07)	0.82(0.06)
1	3.05e-3(4.49e-5)	25.24(0.06)	0.81(0.05)
5	3.03e-3(2.80e-5)	25.26(0.04)	0.80(0.04)
10	3.01e-3(2.81e-5)	25.27(0.04)	0.79(0.04)
50	3.07e-3(3.95e-5)	25.20(0.06)	0.79(0.02)
100	3.11e-3(5.96e-5)	25.15(0.06)	0.80(0.02)
500	3.17e-3(5.83e-5)	25.01(0.07)	0.78(0.04)
10000	3.17e-3(2.90e-5)	25.03(0.04)	0.79(0.04)

References

- Agostinelli F, Anderson M, Lee H (2013) Adaptive multi-column deep neural networks with application to robust image denoising. In: Advances in Neural Information Processing Systems, pp 1493–1501
- Aharon M, Elad M, Bruckstein A (2006) K-SVD: An algorithm for designing overcomplete dictionaries for sparse representation. *IEEE Transactions on Signal Processing* 54(11):4311–4322
- Arjovsky M, Chintala S, Bottou L (2017) Wasserstein Generative Adversarial Networks. In: Proceeding of the International Conference on Machine Learning, pp 214–223
- Bae B, Feklistov A, Lass-Napiorkowska A, Landick R, Darst S (2015) Structure of a bacterial RNA polymerase holoenzyme open promoter complex. *Elife* 4:e08504
- Bai XC, McMullan G, Scheres S (2015) How Cryo-EM is revolutionizing structural biology. *Trends in Biochemical Sciences* 40(1):49–57
- Baldi P (2012) Autoencoders, unsupervised learning, and deep architectures. In: Proceedings of ICML workshop on unsupervised and transfer learning, JMLR Workshop and Conference Proceedings, pp 37–49
- Bau D, Zhu JY, Wulff J, Peebles W, Strobel H, Zhou B, Torralba A (2019) Seeing what a gan cannot generate. In: Proceedings of the IEEE/CVF International Conference on Computer Vision, pp 4502–4511
- Bhamre T, Zhang T, Singer A (2016) Denoising and covariance estimation of single particle Cryo-EM images. *Journal of Structural Biology* 195(1):72–81
- Browning D, Busby S (2004) The regulation of bacterial transcription initiation. *Nature Reviews Microbiology* 2(1):57–65
- Chen J, Chen J, Chao H, Yang M (2018) Image blind denoising with generative adversarial network based noise modeling. In: Proceedings of the IEEE Conference on Computer Vision and Pattern Recognition, pp 3155–3164
- Chen J, Chiu C, Gopalkrishnan S, Chen A, Olinares P, Saecker R, Winkelman J, Maloney M, Chait B, Ross W, et al. (2020) Stepwise promoter melting by bacterial RNA polymerase. *Molecular Cell*
- Cox M, Cox T (2008) Multidimensional scaling. In: Handbook of data visualization, Springer, pp 315–347
- Dabov K, Foi A, Katkovnik V, Egiazarian K (2007) Image denoising by sparse 3-D transform-domain collaborative filtering. *IEEE Transactions on Image Processing* 16(8):2080–2095
- Dai Z, Yang Z, Yang F, Cohen WW, Salakhutdinov R (2017) Good semi-supervised learning that requires a bad gan. In: Proceedings of the 31st International Conference on Neural Information Processing Systems, pp 6513–6523
- Dong Z, Liu G, Ni G, Jerwick J, Duan L, Zhou C (2020) Optical coherence tomography image denoising using a generative adversarial network with speckle modulation. *Journal of Biophotonics* 13(4):e201960135
- Frank J (2006) Three-dimensional electron microscopy of macromolecular assemblies: visualization of biological molecules in their native state. Oxford University Press

- Gao C, Liu J, Yao Y, Zhu W (2019) Robust estimation and generative adversarial nets. In: International Conference on Learning Representation, New Orleans Louisiana, USA
- Gao C, Yao Y, Zhu W (2020) Generative adversarial nets for robust scatter estimation: A proper scoring rule perspective. *Journal of Machine Learning Research* 21:160–1
- Goodfellow I, Pouget-Abadie J, Mirza M, Xu B, Warde-Farley D, Ozair S, Courville A, Bengio Y (2014) Generative adversarial nets. In: *Advances in Neural Information Processing Systems*, pp 2672–2680
- Gu H, Unarta IC, Huang X, Yao Y (2020) Robust autoencoder gan for cryo-em image denoising
- Gulrajani I, Ahmed F, Arjovsky M, Dumoulin V, Courville A (2017) Improved training of Wasserstein GANs. In: *Advances in Neural Information Processing Systems*, pp 5767–5777
- Hua Y, Li R, Zhao Z, Chen X, Zhang H (2019) Gan-powered deep distributional reinforcement learning for resource management in network slicing. *IEEE Journal on Selected Areas in Communications* 38(2):334–349
- Huber P (1992) Robust estimation of a location parameter. In: *Breakthroughs in Statistics*, Springer, pp 492–518
- Karras T, Aila T, Laine S, Lehtinen J (2018) Progressive growing of gans for improved quality, stability, and variation. In: *International Conference on Learning Representation*, Vancouver, Canada
- Kenzaki H, Koga N, Hori N, Kanada R, Li W, Okazaki K, Yao XQ, Takada S (2011) CafeMol: A coarse-grained biomolecular simulator for simulating proteins at work. *Journal of Chemical Theory and Computation* 7(6):1979–1989
- Kingma DP, Ba J (2015) Adam: A method for stochastic optimization. In: *International Conference on Learning Representation*, San Diego, California, USA
- Krivov G, Shapovalov M, Dunbrack Jr RL (2009) Improved prediction of protein side-chain conformations with SCWRL4. *Proteins: Structure, Function, and Bioinformatics* 77(4):778–795
- Krull A, Buchholz TO, Jug F (2019) Noise2void-learning denoising from single noisy images. In: *Proceedings of the IEEE Conference on Computer Vision and Pattern Recognition*, pp 2129–2137
- Kühlbrandt W (2014) The resolution revolution. *Science* 343(6178):1443–1444
- Lehtinen J, Munkberg J, Hasselgren J, Laine S, Karras T, Aittala M, Aila T (2018) Noise2noise: Learning image restoration without clean data. In: *Proceeding of the International Conference on Machine Learning*, pp 2965–2974
- Maaten L, Hinton G (2008) Visualizing data using t-SNE. *Journal of Machine Learning Research* 9(11):2579–2605
- Marabini R, Masegosa I, San Martín M, Marco S, Fernandez J, De la Fraga L, Vaquerizo C, Carazo J (1996) Xmipp: an image processing package for electron microscopy. *Journal of Structural Biology* 116(1):237–240
- Moore B, Kelley L, Barber J, Murray J, MacDonald J (2013) High-quality protein backbone reconstruction from alpha carbons using Gaussian mixture models. *Journal of Computational Chemistry* 34(22):1881–1889
- Murakami K, Masuda S, Darst S (2002) Structural basis of transcription initiation: Rna polymerase holoenzyme at 4 Å resolution. *Science* 296(5571):1280–1284
- Ng A, Jordan M, Weiss Y (2002) On spectral clustering: Analysis and an algorithm. In: *Advances in Neural Information Processing Systems*, pp 849–856
- Okazaki K, Koga N, Takada S, Onuchic J, Wolynes P (2006) Multiple-basin energy landscapes for large-amplitude conformational motions of proteins: Structure-based molecular dynamics simulations. *Proceedings of the National Academy of Sciences* 103(32):11844–11849
- Punjani A, Rubinstein JL, Fleet DJ, Brubaker MA (2017) CryoSPARC: algorithms for rapid unsupervised Cryo-EM structure determination. *Nature Methods* 14(3):290
- Quan Y, Chen M, Pang T, Ji H (2020) Self2self with dropout: Learning self-supervised denoising from single image. In: *Proceedings of the IEEE/CVF Conference on Computer Vision and Pattern Recognition*, pp 1890–1898

- Sarmad M, Lee HJ, Kim YM (2019) Rl-gan-net: A reinforcement learning agent controlled gan network for real-time point cloud shape completion. In: Proceedings of the IEEE/CVF Conference on Computer Vision and Pattern Recognition, pp 5898–5907
- Scheres S (2016) Processing of structurally heterogeneous Cryo-EM data in RELION. In: Methods in Enzymology, vol 579, Elsevier, pp 125–157
- Shen P (2018) The 2017 Nobel Prize in Chemistry: Cryo-EM comes of age. Analytical and Bioanalytical Chemistry 410(8):2053–2057
- Su M, Zhang H, Schawinski K, Zhang C, Cianfrocco M (2018) Generative adversarial networks as a tool to recover structural information from cryo-electron microscopy data. BioRxiv p 256792
- Tenenbaum J, De Silva V, Langford J (2000) A global geometric framework for nonlinear dimensionality reduction. Science 290(5500):2319–2323
- Tran L, Nguyen SM, Arai M (2020) GAN-based noise model for denoising real images. In: Proceedings of the Asian Conference on Computer Vision
- Tripathi S, Lipton ZC, Nguyen TQ (2018) Correction by projection: Denoising images with generative adversarial networks
- Vincent P, Larochelle H, Bengio Y, Manzagol PA (2008) Extracting and composing robust features with denoising autoencoders. In: Proceeding of the International Conference on Machine Learning, pp 1096–1103
- Wang F, Gong H, Liu G, Li M, Yan C, Xia T, Li X, Zeng J (2016) DeepPicker: A deep learning approach for fully automated particle picking in Cryo-EM. Journal of Structural Biology 195(3):325–336
- Wang J, Yin CC (2013) A zernike-moment-based non-local denoising filter for cryo-em images. Science China Life Sciences 56(4):384–390
- Wang Z, Bovik A, Sheikh H, Simoncelli E (2004) Image quality assessment: from error visibility to structural similarity. IEEE Transactions on Image Processing 13(4):600–612
- Warren BE (1990) X-ray Diffraction. Courier Corporation
- Wei DY, Yin CC (2010) An optimized locally adaptive non-local means denoising filter for cryo-electron microscopy data. Journal of Structural Biology 172(3):211–218
- Wong W, Bai XC, Brown A, Fernandez I, Hanssen E, Condrón M, Tan YH, Baum J, Scheres S (2014) Cryo-EM structure of the Plasmodium falciparum 80s ribosome bound to the anti-protozoan drug emetine. Elife 3:e03080
- Wüthrich K (1986) Nmr with proteins and nucleic acids. Europhysics News 17(1):11–13
- Xian Y, Gu H, Wang W, Huang X, Yao Y, Wang Y, Cai JF (2018) Data-driven tight frame for cryo-em image denoising and conformational classification. In: Proceeding of the IEEE Global Conference on Signal and Information Processing (GlobalSIP), pp 544–548
- Xie J, Xu L, Chen E (2012) Image denoising and inpainting with deep neural networks. In: Advances in Neural Information Processing Systems, pp 341–349
- Yang Q, Yan P, Zhang Y, Yu H, Shi Y, Mou X, Kalra M, Zhang Y, Sun L, Wang G (2018) Low-dose CT image denoising using a generative adversarial network with wasserstein distance and perceptual loss. IEEE Transactions on Medical Imaging 37(6):1348–1357
- Zhang K, Zuo W, Chen Y, Meng D, Zhang L (2017) Beyond a gaussian denoiser: Residual learning of deep CNN for image denoising. IEEE Transactions on Image Processing 26(7):3142–3155
- Zhong E, Bepler T, Davis J, Berger B (2020) Reconstructing continuous distributions of 3D protein structure from Cryo-EM images. In: International Conference on Learning Representation, Addis Ababa, Ethiopia